

Diffusion Models Generalize but Not in the Way You Might Think

Tim Kaiser¹ and Markus Kollmann¹

Heinrich-Heine-University Düsseldorf

Abstract. Standard evaluation metrics suggest that Denoising Diffusion Models based on U-Net or Transformer architectures generalize well in practice. However, as it can be shown that an optimal Diffusion Model fully memorizes the training data, the model error determines generalization. Here, we show that although sufficiently large denoiser models show increasing memorization of the training set with increasing training time, the resulting denoising trajectories do not follow this trend. Our experiments indicate that the reason for this observation is rooted in the fact that overfitting occurs at intermediate noise levels, but the distribution of noisy training data at these noise levels has little overlap with denoising trajectories during inference. To gain more insight, we make use of a 2D toy diffusion model to show that overfitting at intermediate noise levels is largely determined by model error and the density of the data support. While the optimal denoising flow field localizes sharply around training samples, sufficient model error or dense support on the data manifold suppresses exact recall, yielding a smooth, generalizing flow field. To further support our results, we investigate how several factors, such as training time, model size, dataset size, condition granularity, and diffusion guidance, influence generalization behavior.

Keywords: Generative Models · Diffusion · Memorization · Generalization · Image Generation · Flow · Model Error · EDM

1 Introduction

The goal of generative modeling is to sample from an unknown data distribution, given a finite subset of samples from it. Diffusion models have demonstrated a remarkable ability to synthesize novel samples across a range of data modalities, including images [27, 36, 38, 39, 52, 56], video [6, 24, 29, 44, 60], text [45, 47, 61, 63], and audio [31, 32, 40, 42]. At the same time, they are known to occasionally replicate training samples [10, 23, 48, 54], something particularly problematic for large Text-to-Image models [41] and critical in, for example, medical applications [13, 16, 17]. In classical Deep Learning, memorizing the training data is not necessarily a concern, as long as the test performance improves alongside it. However, many works have found memorization and generalization to be mutually exclusive for diffusion models [7, 8, 22, 62, 64]. Supporting this notion, optimal diffusion models are unable to sample anything other than the training

data [2,21,50], raising the question of how diffusion models generalize rather than how they memorize. It is known that smoothing the geometry of the flow field of optimal diffusion enables the generalization of novel samples [50] and that model regularization, inductive biases, and training dynamics affect the transition between generalization and memorization [7,35,51]. Supplementing that, this work provides extensive empirical evidence that there is a strong link between memorization and model error, explains the mechanism behind the transition from memorization to generalization as a function of model error, and shows that regular diffusion inference avoids memorization occurring at intermediate noise levels, thereby preserving generalization. Our main contributions can be summarized as follows:

- We identify a substantial gap between the training and validation performance of state-of-the-art diffusion models on the denoising objective model’s are trained on. The gap scales with longer training time, larger model size, and smaller dataset size. The shape of this gap has a characteristic peak at intermediate noise levels and is robust across a variety of model settings.
- We demonstrate, using a 2D toy model, that the shape and magnitude of this gap are determined by the geometry of the learned flow field, which depends on the model error and the density of the data distribution’s support. If the model error is small enough and/or the data manifold is sparsely supported, the flow field localizes sharply around individual training samples, leading to a large gap between training and validation performance. If the model error is sufficiently large and/or the data manifold is densely supported, the flow field around the data manifold is significantly smoothed, thereby suppressing the gap.
- Lastly, we show that there are qualitative differences in generalization behavior between diffusion training and diffusion inference. Specifically, the aforementioned gap diminishes when we replace the forward noising process of the training objective with random trajectories from regular diffusion inference, stopped at the desired noise level.

All code will be released upon publication.

2 Related work

Diffusion models were developed in their current form from two different starting points: via variational inference with an objective resembling denoising score matching [27], and directly via denoising score matching, applied to stochastic differential equations [55,56]. Several improvements, including architectural advances [14], sampling techniques such as guidance [14], and latent diffusion [49], have established diffusion models as the dominant class of generative models. The present work uses the EDM-framework, which, in both iterations, achieved state-of-the-art performance in the class-conditional setting, owing to a comprehensive suite of analyses and improvements to the training and sampling of diffusion models [36,38].

Understanding generalization in diffusion models. Recently, analytical formulations of optimal diffusion models appeared, showing that they are unable to sample anything but the training data [2, 21, 50], a stark contrast to the classical view on memorization, where a fully memorizing model can technically still generalize perfectly. This perspective, in light of the manifold hypothesis [20], sparked a series of works analyzing the relationship between optimal diffusion and well-generalizing real diffusion models. They establish that the optimal flow field has a sharp geometry around the training samples [21, 59] and that smoothing this geometry plays a key role for successful generalization [1, 18, 50]. Another, related perspective, is to consider the sampling process in distinct phases with respect to noise level, typically assigning the strongest memorization behavior to the last phase, as here optimal diffusion collapses onto the data support [5, 59]. Next to the mechanism itself, many works have investigated the factors that influence it, most prominently training time [7], dataset size [25] and model complexity, but also found more unexpected factors such as the difference in training loss between models [8], the number of noise samples per data sample [22] and the model condition [23]. In addition to the explicit configuration of diffusion models, their inductive biases might implicitly promote generalization, akin to the smoothing behavior mentioned above. Works have identified locality [43] and equivariance [35] biases from both data statistics and the architecture, a bias towards geometry-adaptive harmonic bases, adapted to the underlying images [34], and implicit regularization [19] as biases with significant influence on the generalization ability of diffusion models.

Text-to-Image models. The consequences of memorization in diffusion models are especially prevalent in Text-to-Image Models, due to legal and privacy concerns. Works here present extensive documentation of different kinds of memorization behavior, from full replicas to mosaic-like reuse of training patterns, as well as a range of methods and tricks to mitigate them [10, 11, 15, 51, 53, 54].

The role of metrics. Memorization and overfitting are of growing concern for the performance-oriented literature on diffusion models, where they have largely been absent from the discussion. As quantitative phenomena, they depend on the metric that is used to measure them. This proves to be a difficult task, as established generative metrics are focused on measuring fidelity and diversity, not novelty, [33], and memorization-specific metrics are unable to distinguish it from overfitting [57, 58]. It is therefore crucial to consider the role of the metric in understanding memorization and generalization.

3 Better performing diffusion models show a larger generalization gap

To quantify overfitting (Fig. 1) we compute the **relative generalization gap** G when reconstructing clean data points $\{\mathbf{y}_i\}_{i=1}^N$ from noisy data points $\mathbf{x}_i(\sigma) = \mathbf{y}_i + \sigma\eta_i$, $\eta_i \sim \mathcal{N}(0, I)$, at noise level σ :

$$G(\sigma) = \frac{E_{val}(\sigma) - E_{train}(\sigma)}{E_{train}(\sigma)},$$

where $E_{\mathcal{D}}(\sigma)$, with $\mathcal{D} \in \{\mathcal{D}_{train}, \mathcal{D}_{val}\}$ is the average L2-reconstruction error

$$E_{\mathcal{D}}(\sigma) = \frac{1}{N} \sum_i \|y_i^{\mathcal{D}} - D(x_i^{\mathcal{D}}(\sigma), \sigma)\|_2^2,$$

using the denoiser D . This directly probes a model’s performance on the denoising task it is trained on, rather than comparing fully denoised data, as standard generative metrics such as FID do. We will further investigate this distinction in Sec. 5. Perhaps unsurprisingly, given that an optimal denoiser is overfitting,

we find that state-of-the-art denoiser models exhibit a significant relative generalization gap between training and validation data (Fig. 2). This behavior is consistent across all models and datasets we tested. We use the pretrained EDM2 [38] models to carry out experiments on ImageNet and pretrained as well as re-trained EDM [36] models to carry out experiments on CIFAR-10 and CIFAR-100. The hyperparameters are as reported in [36, 38], unless specified otherwise. Additional results for these models and datasets are available in the supplementary material.

We observe that the relative generalization gap scales with longer training, larger model size, and smaller dataset size. In general, a large gap indicates that a model exhibits different reconstruction performance on training and validation data for a given noise scale. Note that this metric directly probes the model’s denoising performance. In addition to a substantial generalization gap, we observe

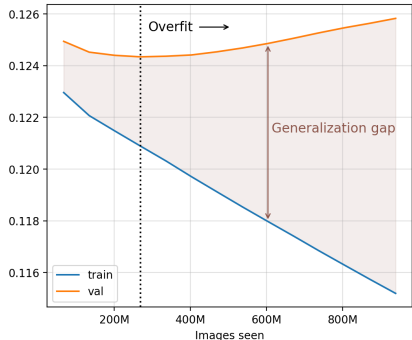


Fig. 1: Generalization gap and overfitting for $E_{\mathcal{D}}(\sigma)$ at $\sigma \approx 1.67$. We define overfitting as a decrease in validation performance while training performance improves.

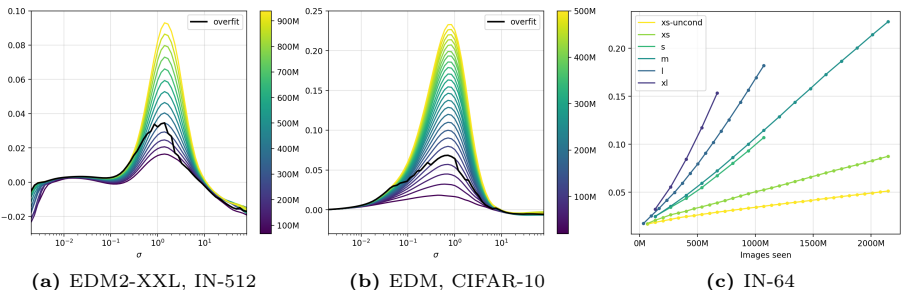


Fig. 2: The relative generalization gap $(E_{val} - E_{train})/E_{train}$ increases with images seen during training (colorbar in millions) and with model size in relation to dataset size. The black line indicates the beginning of overfitting (validation error starts increasing, Fig. 1) for each noise level σ .

classical overfitting: during continued training, validation performance degrades (Fig. 1, Fig. 2, black line), while training performance improves. Crucially, both the relative generalization gap and the overfitting regime are primarily present at intermediate noise levels and sharply drop outside of this range. This observation raises the question of how the relative generalization gap arises and how samples generated with regular diffusion inference are affected by this.

4 How do diffusion models generalize?

To understand the mechanism behind the noise-dependent relative generalization gap observed in Sec. 3, we study a 2D toy diffusion model, following [2].

Consider a symmetric distribution of N training points $\{\mathbf{y}_i^{tr}\}_{i=1}^N$ and N validation points $\{\mathbf{y}_i^{val}\}_{i=1}^N$ along a circle, alternating between each other. The shape of a circle was chosen for two reasons: It mimics the hyperplane of high-dimensional data distributions, and the superposition of samples lies far outside the data manifold, avoiding denoising interactions that are not possible in high-dimensional space. The symmetric distribution of points was chosen for clarity. The results of this section are qualitatively unchanged for a random distribution on the circle. See supplementary material for more details.

Consider the time variable $t \in [0, 1]$ and the current noise level $\sigma := \sigma(t)$, with $\sigma(0) = 0$ and $\sigma(1) \gg std(\mathbf{y}_i)$. Denote $\mathbf{x} := \mathbf{x}(t)$ a point along a denoising trajectory. Then, the **optimal target predictor** in the Bayesian sense is given by the posterior mean of the data distribution $\{\mathbf{y}_i^{tr}\}_{i=1}^N$ [2]

$$\mathbf{y}^*(\mathbf{x}, \sigma) = \frac{\sum_i \mathbf{y}_i^{tr} N(\mathbf{x} | \mathbf{y}_i^{tr}, \sigma^2)}{\sum_i N(\mathbf{x} | \mathbf{y}_i^{tr}, \sigma^2)} \quad (1)$$

This defines a smooth vector field over \mathbb{R}^2 whose geometry depends on σ : For large σ , it globally tends towards the superposition of all training points. For small σ , the vector field collapses to a projection onto the nearest training sample, and for intermediate σ , a mixture of the above (Fig. 3). Sampling randomly initialized trajectories with this predictor yields perfect memorization of the training set. Note that the conditional optimal predictor is the same as \mathbf{y}^* , but the posterior mean only includes training points with the given condition.

To simulate real, erroneous diffusion models, we construct an **error-prone target predictor** by substituting the real data distribution $P(\mathbf{y})$ with an "uncertain" data distribution $P_\delta(\mathbf{y}) = \int_{\mathbb{R}^d} \mathcal{N}(\mathbf{y} | \mathbf{y}', \delta^2) P(\mathbf{y}') d\mathbf{y}'$, where the true data points are randomly shifted by isotropic Gaussian noise with variance δ^2 . Therefore, their exact locations are unknown to the predictor. The corresponding posterior mean is

$$\mathbf{y}_\delta(\mathbf{x}, \sigma) = \frac{\delta^2 \mathbf{x} + \sigma^2 \mathbf{y}^*(\mathbf{x}, \tilde{\sigma})}{\sigma^2 + \delta^2}, \quad \tilde{\sigma}^2 = \sigma^2 + \delta^2. \quad (2)$$

with $\mathbf{y}^* = \mathbf{y}_0$ [2]. The prediction error decomposes naturally into two factors:

$$\mathbf{y}_\delta(\mathbf{x}, \sigma) - \mathbf{x} = \frac{\sigma^2}{\sigma^2 + \delta^2} (\mathbf{y}^*(\mathbf{x}, \tilde{\sigma}) - \mathbf{x}), \quad (3)$$

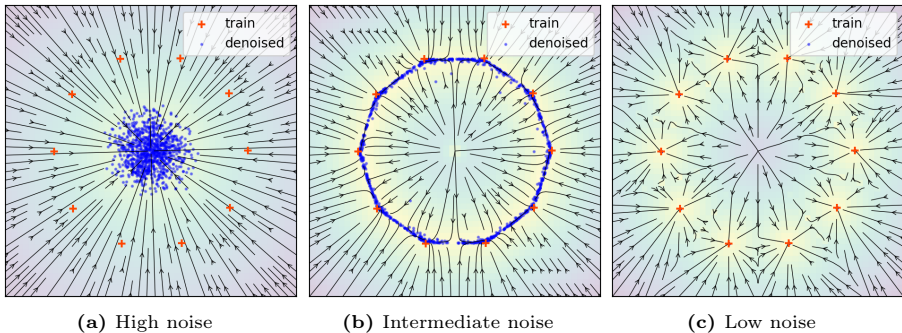


Fig. 3: Flow field lines and predictions of the optimal target predictor $\mathbf{y}^*(\mathbf{x}, \sigma)$ at different noise levels $\sigma = 28, 2.8, 0.63$. Color indicates the magnitude of the prediction error $\mathbf{y}^*(\mathbf{x}, \sigma) - \mathbf{x}$. Field geometry is (a) global, predictions tend towards the superposition of all training points, (b) moderately localized around training points, predictions approximate the data manifold, and (c) highly localized around each training point, predictions replicate the training points.

which separate geometry, determined by the arrangement of training points and the scale $\tilde{\sigma}$, and dynamics, $\frac{\sigma^2}{\sigma^2 + \delta^2}$, a scalar that controls how strongly this geometry is expressed. Interestingly, when quantifying the relative generalization gap in this toy model, using the same protocol as in Sec. 3, we not only find that it is present but also the same characteristic peak at intermediate noise levels (Fig. 4).

Analyzing the behavior of \mathbf{y}_δ at different regimes of the ratio σ/δ explains why the peak emerges:

At high noise ($\sigma \gg \delta$), \mathbf{y}_δ behaves like the posterior mean predictor \mathbf{y}^* , but noisy samples \mathbf{x} are far away from the data manifold. Predictions tend towards the superposition of the training data, regardless of \mathbf{y} being a training or validation sample, resulting in similar average errors between training and validation samples.

At low noise ($\sigma \ll \delta$), the prefactor $\frac{\sigma^2}{\sigma^2 + \delta^2}$ dampens the dynamics, causing \mathbf{y}_δ to behave identity-like ($\mathbf{y}_\delta(\mathbf{x}, \sigma) \approx \mathbf{x}$). In addition, the flow field localizes more slowly around training points, because \mathbf{y}^* is evaluated at $\tilde{\sigma}$ and not at σ . Again, average errors are very similar.

At intermediate noise ($\sigma \approx \delta$), neither are dynamics suppressed nor are samples far off the manifold. Crucially, the error parameter δ determines *where in the flow field the transition from ($\sigma \gg \delta$) to ($\sigma \ll \delta$) happens*. For large δ , the

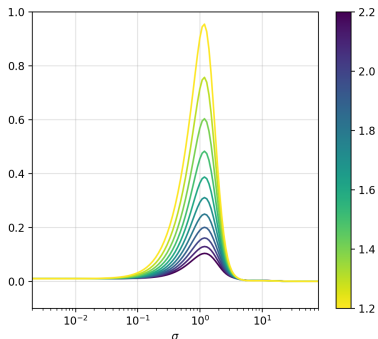


Fig. 4: Relative generalization gap $(E_{val} - E_{train})/E_{train}$ in our 2D toy model for different settings of the model error parameter δ (colorbar).

generalization gap never emerges because the predictor transitions from global averaging to identity-like behavior without ever entering highly localized regions of the flow field. For sufficiently small δ , a generalization gap emerges at $\sigma \approx \delta$, because $\mathbf{x}(t)$ is close enough to the data manifold for the posterior mean to be attracted to the specific locations of training points, and the prefactor does not yet suppress the dynamics.

To visualize how δ affects the relative generalization gap, we compute it for each point in space, treating that point as the validation set. The resulting contours show how quickly the gap increases as we move away from training points (Fig. 5).

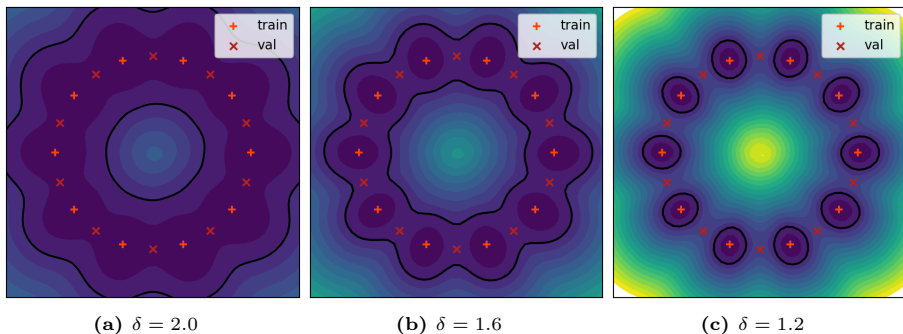


Fig. 5: Filled contours showing the relative generalization gap $(E - E_{train})/E_{train}$ at intermediate noise ($\sigma \approx 1.1$) between the training points and each point in space, respectively. The black lines enclose the area where this gap is 0.5 or less. As the model error δ decreases, this region shrinks until it no longer contains the validation points, indicating that the generalization gap to the validation set is larger than 0.5.

The scale of the generalization gap is determined by the geometry around training points, hence it is also influenced by the density of training points on the manifold. The results in Fig. 2 suggested this with the much smaller CIFAR datasets showing significantly higher levels of overfit than the larger ImageNet dataset, especially when comparing models with a similar number of parameters. Accordingly, a denser distribution of training points on the manifold shows a significantly reduced gap in the toy model. This also suggests that condition granularity amplifies the gap, since in the toy model it’s equivalent to reducing the dataset to a specific subset.

5 Overfit in reconstruction does not imply overfit in inference

In practice, well-performing diffusion models are evaluated using Fréchet Distance-based metrics: the Fréchet Inception Distance (FID), with Inception-v3 fea-

tures [26], and, more recently, the Fréchet DINOv2 Distance (FDD), with DINOv2 features [46]. As the main goal of generative models is distributional similarity, it has long been standard practice to use the much larger training set, or all available data, as the reference for these metrics rather than the validation set. Consequently, in the overfit regime, the metrics may differ depending on the choice of the reference data set. In this section, we systematically investigate how different metrics are related to a model’s generalization performance. To this end, we repeat the analysis of Sec. 3 and incrementally adjust the metric to go from our L2-reconstruction-error-based metric from Sec. 3 to the standard FDD/FID, isolating the influence of each factor along the way (Tab. 1). We extend the definition of the generalization gap to different metrics M :

$$G = \frac{M_{val} - M_{train}}{M_{val}},$$

with $M_{train/val}$ being a metric on the distribution level (Fréchet Distance) or sample level (L2-reconstruction error) operating either in pixel space or feature space. As Inception-v3 has known shortcomings [57], we will use DINOv2 features for the rest of this work. See the supplementary material for the corresponding results with Inception-v3. To enable comparisons with tFD, which is the standard metric to quantify generative performance and does not depend on σ , we fix σ for the reconstruction-based metrics near the peak of the generalization gap.

Table 1: Overview of metric configurations we use for comparisons in Sec. 5. Each metric differs from the previous in one design choice. Feature space here refers to DINOv2 or Inception-v3.

Metric M	Space	Distance	Sampling Method
rL2 _{pix} (from Sec. 3)	Pixel	Avg. L2	One-step reconstruction
rL2 _{feat}	Feature	Avg. L2	One-step reconstruction
rFD	Feature	Fréchet Dist.	One-step reconstruction
tFD (FDD/FID)	Feature	Fréchet Dist.	Denosing trajectory

Starting with the relative generalization gap in pixel space (rL2_{pix}), we find a constant increase with training time and model size (Fig. 2c). Applying a feature extractor, such as DINOv2 or Inception-v3, to the denoised and clean data samples does not qualitatively affect this behavior (Fig. 6a), indicating that memorization occurs at all abstraction levels from local pixel correlations to image semantics. Surprisingly, for one-step reconstructions, both the average L2-distance between samples and the Fréchet Distance between distributions yield the same qualitative increase of the gap with respect to training time and model size (Fig. 6b). Hence, even the statistics of feature distributions, as measured by the Fréchet Distance, seem to overfit to a similar extent as individual samples. Only for a multi-step denoising trajectory, starting from pure noise, we observed saturating or even decreasing generalization gaps with

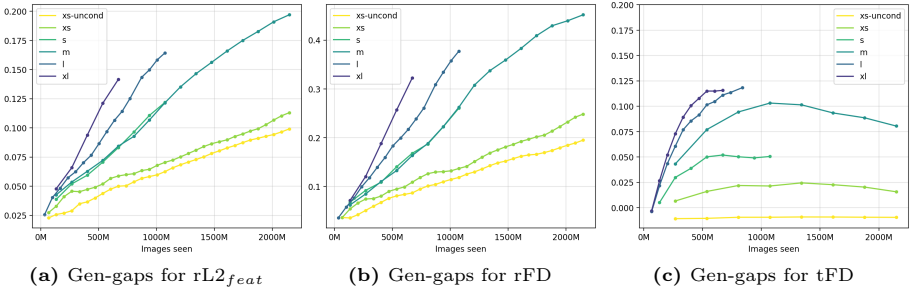


Fig. 6: Relative generalization gaps $(M_{val} - M_{train})/M_{train}$ vs training time and model capacity for various metrics on ImageNet-64. Approximately linearly scaling for one-step reconstruction metrics, using (a) L2-norm to compare paired samples, (b) Fréchet Distance to compare distributions of paired samples. (c) Relative generalization gaps using tFD (FDD) as a metric, comparing the output of denoising trajectories instead of one-step predictions. (a) and (b) show results for σ near the peaks in their generalization gaps.

increasing training time (Fig. 6c). Moreover, not only the generalization gap but also tFD_{train} and tFD_{val} show different behaviour in comparison to the other metrics (Fig. 7), indicating that this form of generalization is a property of the denoising trajectories. When following the random denoising trajectories only up to an intermediate noise level and then forcing a one-step prediction, just like in the reconstruction-error setting, the generalization gap remains small, and the result is similar to Fig. 6c. This isolates the distribution of noisy samples $\mathbf{x}(t)$ at noise level σ as the crucial difference between the metrics, changing generalization behavior. The reconstruction-based metrics use isotropic Gaussian clouds around data points, while the denoising trajectories generated by regular

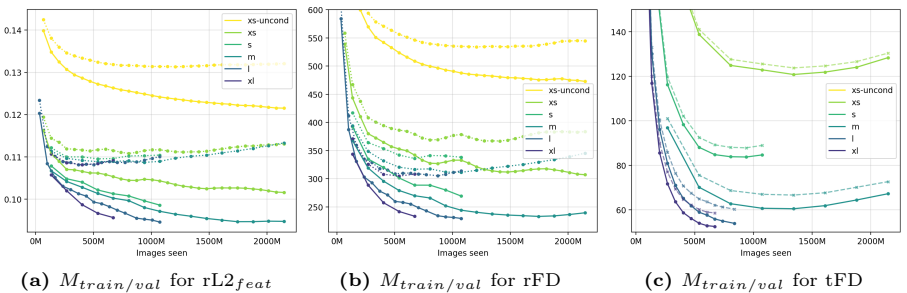


Fig. 7: Metric results for M_{train} and M_{val} for various metrics on ImageNet-64. (a),(b) For reconstruction-based metrics, the training performance improves with training time and model size, whereas the validation performance eventually degrades, resulting in classical overfit behavior. (c) With FDD, overfitting is absent, because training performance degrades as well.

inference approach the data points in a highly non-isotropic way, preserving generalization.

The increase in the generalization gap induced by model size is consistent across all metrics we tested, though less pronounced for tFD. Notably, larger model size improves both M_{train} and M_{val} for all metrics and at any point during training. Curiously, we found that some of the smallest model variants, as well as the EDM models on CIFAR-10 and CIFAR-100, performed better on the validation set than on the training set (Fig. 6c). We hypothesize that due to the lack of overfitting, the generalization gap is determined by the misalignment of feature statistics between the training and validation splits, and that the feature statistics of the generated samples coincidentally align more closely with those of the validation split in this setting.

5.1 Strong conditioning amplifies memorization

Due to the high dimensionality of spaces in which diffusion models operate, they contain many regions in which the data manifold is sparsely supported. The data samples in these regions tend to be memorized and are not significantly less likely under the model than other data samples [9]. This effect is exacerbated when modelling a conditional distribution, since it is supported by an even smaller subset of the dataset. Thus, model conditioning should amplify memorization, and the more specific the conditioning, the stronger the memorization, with text-to-image models being an extreme case. To test this, we retrained EDM [36] on CIFAR-10 for 100M images across varying numbers of classes. Classes were computed algorithmically using k-means clustering in DINOv2 feature space.

When comparing paired samples in pixel space ($rL2_{pix}$), an increasingly granular model condition indeed exhibits a moderately increased generalization gap (Fig. 8a). Additionally, this increase is more pronounced at higher noise levels and disappears entirely at lower noise levels, indicating that the condition

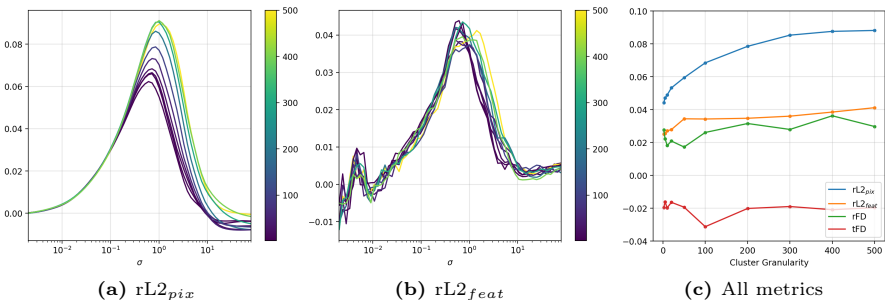


Fig. 8: (a) The relative generalization gap $(M_{val} - M_{train})/M_{train}$ in pixel space increases and shifts to the right when the number of classes (colorbar) for a class-conditioned model increases. (b) In feature space, this trend is mostly mitigated, and (c) stays absent with Fréchet Distance-based metrics. σ fixed near the peak of the gap.

primarily guides the early stages of the generation process. This is consistent with the toy model, though the effect here is weaker, likely because, unlike in the toy model, the conditional predictors are not independent across conditions. Although the right-shift remains visible, the increase in the generalization gap appears to be mitigated when comparing features of paired samples ($rL2_{feat}$) rather than directly comparing the images (Fig. 8b). Comparing the distributions of paired samples with the Fréchet Distance exhibits the same qualitative behavior (Fig. 8c). It is unclear whether this is a consequence of using features rather than images or whether the additional noise in the evaluation pipeline with features obscures the trend.

5.2 Diffusion guidance

Diffusion guidance is a sampling technique that enhances sample quality by correcting biases in the diffusion model using an auxiliary diffusion model that exhibits these biases even more strongly [2]. Some methods use this to correct specific biases [2, 4, 30], others to accentuate biases, like the popular Classifier-Free Guidance (CFG) [28], which accentuates the model condition by using an unconditional model. However, the best results (on FDD) are obtained when the auxiliary model is a worse version of the primary model, e.g., by having fewer parameters or less training time (Autoguidance [37]). In other words, when the model error is increased. The predictor obtained by this method is closer to the optimal predictor [2], raising the question of how its generalization behavior is affected. Similarly, since an increased condition granularity leads to a larger generalization gap (Sec. 5.1), at least in pixel space, we expect the same to hold for CFG, because it accentuates the model condition. The toy model predicts

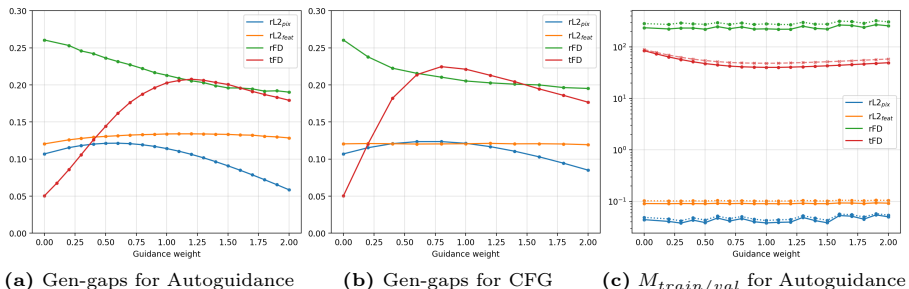


Fig. 9: Relative generalization gaps $(M_{val} - M_{train})/M_{train}$ for Autoguidance and CFG with EDM2-S on ImageNet-64 with varying guidance weights. $w = 0$ corresponds to no guidance. Reconstruction-based metrics fix σ near the peak in the generalization gap.

a moderate yet steady increase in the generalization gap as the guidance weight increases, given that the primary and auxiliary models differ only in their model error δ (see supplementary).

In practice, although tFD significantly improves, it does so at the expense of its generalization gap, and the relative generalization gap with reconstruction-based metrics, surprisingly, shows little to no increase, neither for Autoguidance nor for CFG (Fig. 9). Hence, given a model trained to saturation, guidance affects generalization neither as longer training does nor as increased model size does.

6 Limitations and future work

Our methodology in this work is limited to class-conditional image generation. It is unclear how the interplay between the inductive biases of models and the data modality affects the tradeoff between generalization and memorization, e.g., on text and audio. We used a fully analytical 2D toy model to understand the mechanism behind the generalization gaps we observe in practice. While the low dimensionality enables visualizations, the same calculations can be performed in any number of dimensions. This, together with a more realistic data distribution, would alleviate two of the toy model’s biggest limitations. Beyond methodology, our work posed several open questions:

We identified qualitative differences in the generalization behavior of diffusion training and diffusion inference, i.e., between the reconstruction-based metrics and FDD/FID. While we found that the distribution of noisy samples at intermediate noise levels is the crucial difference between the two settings, it remains unclear why this preserves generalization.

Diffusion guidance, longer training, and larger model size all significantly improve a model’s FDD on both training and validation splits, but all at the expense of a larger relative generalization gap. This suggests that it is not possible to simultaneously improve validation performance and generalization. If true, it is unclear whether this is inherent to the diffusion paradigm or a property of the metric, due to differences in global statistics between the data splits.

Interestingly, FDD does not continue to improve indefinitely as the conditioning becomes more granular. Instead, it attains an optimal value for reasonably granular conditioning [3]. It is unclear whether this is similar to the degradation observed at long training times, due to limitations of the metrics [57], or a separate mechanism inherent to model conditioning.

References

1. Achilli, B., Ventura, E., Silvestri, G., Pham, B., Raya, G., Krotov, D., Lucibello, C., Ambrogioni, L.: Losing dimensions: Geometric memorization in generative diffusion (2024), <https://arxiv.org/abs/2410.08727>
2. Adaloglou, N., Kaiser, T., Iagudin, D., Kollmann, M.: Guiding a diffusion model using sliding windows (2025), <https://arxiv.org/abs/2411.10257>
3. Adaloglou, N., Kaiser, T., Michels, F., Kollmann, M.: Rethinking cluster-conditioned diffusion models for label-free image synthesis (2024), <https://arxiv.org/abs/2403.00570>

4. Ahn, D., Cho, H., Min, J., Jang, W., Kim, J., Kim, S., Park, H.H., Jin, K.H., Kim, S.: Self-rectifying diffusion sampling with perturbed-attention guidance (2025), <https://arxiv.org/abs/2403.17377>
5. Biroli, G., Bonnaire, T., de Bortoli, V., Mézard, M.: Dynamical regimes of diffusion models. *Nature Communications* **15**(1) (Nov 2024). <https://doi.org/10.1038/s41467-024-54281-3>, <http://dx.doi.org/10.1038/s41467-024-54281-3>
6. Blattmann, A., Dockhorn, T., Kulal, S., Mendelevitch, D., Kilian, M., Lorenz, D., Levi, Y., English, Z., Voleti, V., Letts, A., Jampani, V., Rombach, R.: Stable video diffusion: Scaling latent video diffusion models to large datasets (2023), <https://arxiv.org/abs/2311.15127>
7. Bonnaire, T., Urfin, R., Biroli, G., Mézard, M.: Why diffusion models don't memorize: The role of implicit dynamical regularization in training (2025), <https://arxiv.org/abs/2505.17638>
8. Buchanan, S., Pai, D., Ma, Y., Bortoli, V.D.: On the edge of memorization in diffusion models (2025), <https://arxiv.org/abs/2508.17689>
9. van den Burg, G.J.J., Williams, C.K.I.: On memorization in probabilistic deep generative models (2021), <https://arxiv.org/abs/2106.03216>
10. Carlini, N., Hayes, J., Nasr, M., Jagielski, M., Sehwag, V., Tramèr, F., Balle, B., Ippolito, D., Wallace, E.: Extracting training data from diffusion models (2023), <https://arxiv.org/abs/2301.13188>
11. Chen, C., Liu, D., Shah, M., Xu, C.: Exploring local memorization in diffusion models via bright ending attention (2025), <https://arxiv.org/abs/2410.21665>
12. Chong, M.J., Forsyth, D.: Effectively unbiased fid and inception score and where to find them (2020), <https://arxiv.org/abs/1911.07023>
13. Dar, S.U.H., Seyfarth, M., Ayx, I., Papavassiliu, T., Schoenberg, S.O., Siepmann, R.M., Laqua, F.C., Kahmann, J., Frey, N., Baekler, B., Foersch, S., Truhn, D., Kather, J.N., Engelhardt, S.: Unconditional latent diffusion models memorize patient imaging data. *Nature Biomedical Engineering* (2025). <https://doi.org/10.1038/s41551-025-01468-8>, <https://doi.org/10.1038/s41551-025-01468-8>
14. Dhariwal, P., Nichol, A.: Diffusion models beat gans on image synthesis (2021), <https://arxiv.org/abs/2105.05233>
15. Di, J.Z., Lu, Y., Yu, Y., Kamath, G., Dziedzic, A., Boenisch, F.: Demystifying foreground-background memorization in diffusion models (2025), <https://arxiv.org/abs/2508.12148>
16. Dutt, R.: The devil is in the prompts: De-identification traces enhance memorization risks in synthetic chest x-ray generation. *arXiv preprint* (2025), <https://arxiv.org/abs/2502.07516>
17. Dutt, R., Bohdal, O., Sanchez, P., Tsaftaris, S.A., Hospedales, T.: Memcontrol: Mitigating memorization in diffusion models via automated parameter selection. *arXiv preprint* (2024), <https://arxiv.org/abs/2405.19458>
18. Farghly, T., Potapchik, P., Howard, S., Deligiannidis, G., Pidstrigach, J.: Diffusion models and the manifold hypothesis: Log-domain smoothing is geometry adaptive (2025), <https://arxiv.org/abs/2510.02305>
19. Farghly, T., Rebeschini, P., Deligiannidis, G., Doucet, A.: Implicit regularisation in diffusion models: An algorithm-dependent generalisation analysis (2025), <https://arxiv.org/abs/2507.03756>
20. Fefferman, C., Mitter, S., Narayanan, H.: Testing the manifold hypothesis (2013), <https://arxiv.org/abs/1310.0425>
21. Gao, W., Li, M.: How do flow matching models memorize and generalize in sample data subspaces? (2024), <https://arxiv.org/abs/2410.23594>

22. George, A.J., Veiga, R., Macris, N.: Denoising score matching with random features: Insights on diffusion models from precise learning curves (2025), <https://arxiv.org/abs/2502.00336>
23. Gu, X., Du, C., Pang, T., Li, C., Lin, M., Wang, Y.: On memorization in diffusion models (2025), <https://arxiv.org/abs/2310.02664>
24. Gupta, A., Yu, L., Sohn, K., Gu, X., Hahn, M., Li, F.F., Essa, I., Jiang, L., Lezama, J.: Photorealistic video generation with diffusion models. In: Leonardis, A., Ricci, E., Roth, S., Russakovsky, O., Sattler, T., Varol, G. (eds.) *Computer Vision – ECCV 2024*. pp. 393–411. Springer Nature Switzerland, Cham (2025)
25. Halder, I.: A solvable generative model with a linear, one-step denoiser (2025), <https://arxiv.org/abs/2411.17807>
26. Heusel, M., Ramsauer, H., Unterthiner, T., Nessler, B., Hochreiter, S.: Gans trained by a two time-scale update rule converge to a local nash equilibrium (2018), <https://arxiv.org/abs/1706.08500>
27. Ho, J., Jain, A., Abbeel, P.: Denoising diffusion probabilistic models (2020)
28. Ho, J., Salimans, T.: Classifier-free diffusion guidance (2022), <https://arxiv.org/abs/2207.12598>
29. Ho, J., Salimans, T., Gritsenko, A., Chan, W., Norouzi, M., Fleet, D.J.: Video diffusion models (2022)
30. Hong, S.: Smoothed energy guidance: Guiding diffusion models with reduced energy curvature of attention (2024), <https://arxiv.org/abs/2408.00760>
31. Huang, K.P., wen Yang, S., Phan, H., Lu, B.R., Kim, B., Macha, S., Tang, Q., Ghosh, S., yi Lee, H., Kao, C.C., Wang, C.: Impact: Iterative mask-based parallel decoding for text-to-audio generation with diffusion modeling (2025), <https://arxiv.org/abs/2506.00736>
32. Huang, R., Huang, J., Yang, D., Ren, Y., Liu, L., Li, M., Ye, Z., Liu, J., Yin, X., Zhao, Z.: Make-an-audio: Text-to-audio generation with prompt-enhanced diffusion models (2023), <https://arxiv.org/abs/2301.12661>
33. Jiralerspong, M., Bose, A.J., Gemp, I., Qin, C., Bachrach, Y., Gidel, G.: Feature likelihood divergence: Evaluating the generalization of generative models using samples (2024), <https://arxiv.org/abs/2302.04440>
34. Kadkhodaie, Z., Guth, F., Simoncelli, E.P., Mallat, S.: Generalization in diffusion models arises from geometry-adaptive harmonic representations (2024), <https://arxiv.org/abs/2310.02557>
35. Kamb, M., Ganguli, S.: An analytic theory of creativity in convolutional diffusion models (2025), <https://arxiv.org/abs/2412.20292>
36. Karras, T., Aittala, M., Aila, T., Laine, S.: Elucidating the design space of diffusion-based generative models (2022), <https://arxiv.org/abs/2206.00364>
37. Karras, T., Aittala, M., Kynkäänniemi, T., Lehtinen, J., Aila, T., Laine, S.: Guiding a diffusion model with a bad version of itself (2024), <https://arxiv.org/abs/2406.02507>
38. Karras, T., Aittala, M., Lehtinen, J., Hellsten, J., Aila, T., Laine, S.: Analyzing and improving the training dynamics of diffusion models (2024), <https://arxiv.org/abs/2312.02696>
39. Kingma, D.P., Salimans, T., Poole, B., Ho, J.: Variational diffusion models (2023)
40. Kong, Z., Ping, W., Huang, J., Zhao, K., Catanzaro, B.: Diffwave: A versatile diffusion model for audio synthesis (2021)
41. Kowalczyk, A., Hintersdorf, D., Struppek, L., Kersting, K., Dziedzic, A., Boenisch, F.: Finding dori: Memorization in text-to-image diffusion models is not local (2025), <https://arxiv.org/abs/2507.16880>

42. Liu, H., Chen, Z., Yuan, Y., Mei, X., Liu, X., Mandic, D., Wang, W., Plumbley, M.D.: Audioldm: Text-to-audio generation with latent diffusion models (2023), <https://arxiv.org/abs/2301.12503>
43. Lukoianov, A., Yuan, C., Solomon, J., Sitzmann, V.: Locality in image diffusion models emerges from data statistics (2025), <https://arxiv.org/abs/2509.09672>
44. Melnik, A., Ljubljanc, M., Lu, C., Yan, Q., Ren, W., Ritter, H.: Video diffusion models: A survey (2024), <https://arxiv.org/abs/2405.03150>
45. Ochs, S., Habernal, I.: Private synthetic text generation with diffusion models (2024), <https://arxiv.org/abs/2410.22971>
46. Oquab, M., Darcet, T., Moutakanni, T., Vo, H., Szafraniec, M., Khalidov, V., Fernandez, P., Haziza, D., Massa, F., El-Nouby, A., Assran, M., Ballas, N., Galuba, W., Howes, R., Huang, P.Y., Li, S.W., Misra, I., Rabbat, M., Sharma, V., Synnaeve, G., Xu, H., Jegou, H., Mairal, J., Labatut, P., Joulin, A., Bojanowski, P.: Dinov2: Learning robust visual features without supervision (2024), <https://arxiv.org/abs/2304.07193>
47. Popov, V., Vovk, I., Gogoryan, V., Sadekova, T., Kudinov, M.: Grad-tts: A diffusion probabilistic model for text-to-speech (2021)
48. Ren, J., Li, Y., Zeng, S., Xu, H., Lyu, L., Xing, Y., Tang, J.: Unveiling and mitigating memorization in text-to-image diffusion models through cross attention (2025), <https://arxiv.org/abs/2403.11052>
49. Rombach, R., Blattmann, A., Lorenz, D., Esser, P., Ommer, B.: High-resolution image synthesis with latent diffusion models (2022), <https://arxiv.org/abs/2112.10752>
50. Scarvelis, C., de Ocariz Borde, H.S., Solomon, J.: Closed-form diffusion models (2025), <https://arxiv.org/abs/2310.12395>
51. Shah, K., Kalavasis, A., Klivans, A.R., Daras, G.: Does generation require memorization? creative diffusion models using ambient diffusion (2025), <https://arxiv.org/abs/2502.21278>
52. Sohl-Dickstein, J., Weiss, E.A., Maheswaranathan, N., Ganguli, S.: Deep unsupervised learning using nonequilibrium thermodynamics (2015)
53. Somepalli, G., Singla, V., Goldblum, M., Geiping, J., Goldstein, T.: Diffusion art or digital forgery? investigating data replication in diffusion models (2022), <https://arxiv.org/abs/2212.03860>
54. Somepalli, G., Singla, V., Goldblum, M., Geiping, J., Goldstein, T.: Understanding and mitigating copying in diffusion models (2023), <https://arxiv.org/abs/2305.20086>
55. Song, Y., Ermon, S.: Generative modeling by estimating gradients of the data distribution (2020), <https://arxiv.org/abs/1907.05600>
56. Song, Y., Sohl-Dickstein, J., Kingma, D.P., Kumar, A., Ermon, S., Poole, B.: Score-based generative modeling through stochastic differential equations (2021)
57. Stein, G., Cresswell, J.C., Hosseinzadeh, R., Sui, Y., Ross, B.L., Villecroze, V., Liu, Z., Caterini, A.L., Taylor, J.E.T., Loaiza-Ganem, G.: Exposing flaws of generative model evaluation metrics and their unfair treatment of diffusion models (2023), <https://arxiv.org/abs/2306.04675>
58. Theis, L., van den Oord, A., Bethge, M.: A note on the evaluation of generative models (2016), <https://arxiv.org/abs/1511.01844>
59. Ventura, E., Achilli, B., Silvestri, G., Lucibello, C., Ambrogioni, L.: Manifolds, random matrices and spectral gaps: The geometric phases of generative diffusion (2025), <https://arxiv.org/abs/2410.05898>

60. Wang, Y., Chen, X., Ma, X., Zhou, S., Huang, Z., Wang, Y., Yang, C., He, Y., Yu, J., Yang, P., Guo, Y., Wu, T., Si, C., Jiang, Y., Chen, C., Loy, C.C., Dai, B., Lin, D., Qiao, Y., Liu, Z.: Lavie: High-quality video generation with cascaded latent diffusion models (2023), <https://arxiv.org/abs/2309.15103>
61. Xu, M., Geffner, T., Kreis, K., Nie, W., Xu, Y., Leskovec, J., Ermon, S., Vahdat, A.: Energy-based diffusion language models for text generation (2025), <https://arxiv.org/abs/2410.21357>
62. Ye, Z., Zhu, Q., Tao, M., Chen, M.: Provable separations between memorization and generalization in diffusion models (2025), <https://arxiv.org/abs/2511.03202>
63. Yi, Q., Chen, X., Zhang, C., Zhou, Z., Zhu, L., Kong, X.: Diffusion models in text generation: a survey. *PeerJ Computer Science* **10**, e1905 (2024). <https://doi.org/10.7717/peerj-cs.1905>, <https://doi.org/10.7717/peerj-cs.1905>
64. Yoon, T., Choi, J.Y., Kwon, S., Ryu, E.K.: Diffusion probabilistic models generalize when they fail to memorize. In: *ICML 2023 Workshop on Structured Probabilistic Inference & Generative Modeling* (2023), <https://openreview.net/forum?id=shciCbSk9h>

Supplementary Material

A Fréchet Distance (FD) with partial inference (early stopping)

In our experiments, we found a significant difference in the relative generalization gaps between metrics $rL2_{pix}$, $rL2_{feat}$, and rFD, which all behaved similarly, and metric tFD. The step from rFD to tFD is to generate samples via regular diffusion inference rather than reconstructing noisy data samples. To further isolate what causes the difference in generalization behavior, we truncated inference by forcing a one-step prediction from any given noise level σ , just as rFD does. As EDM models use the Heun method for sampling, this can be implemented by omitting the 2nd-order correction and setting the step size to 1. The resulting metric differs from rFD only in the distribution of noisy samples $\mathbf{x}(t)$ at noise level σ . We find that this modified metric exhibits the same saturation in M_{train} , M_{val} and the relative generalization gap that *tFD* does (Fig. 10), confirming that the distribution of noisy samples $\mathbf{x}(t)$ at noise level σ is responsible for this, not the multi-step inference from there down to $\sigma = 0$.

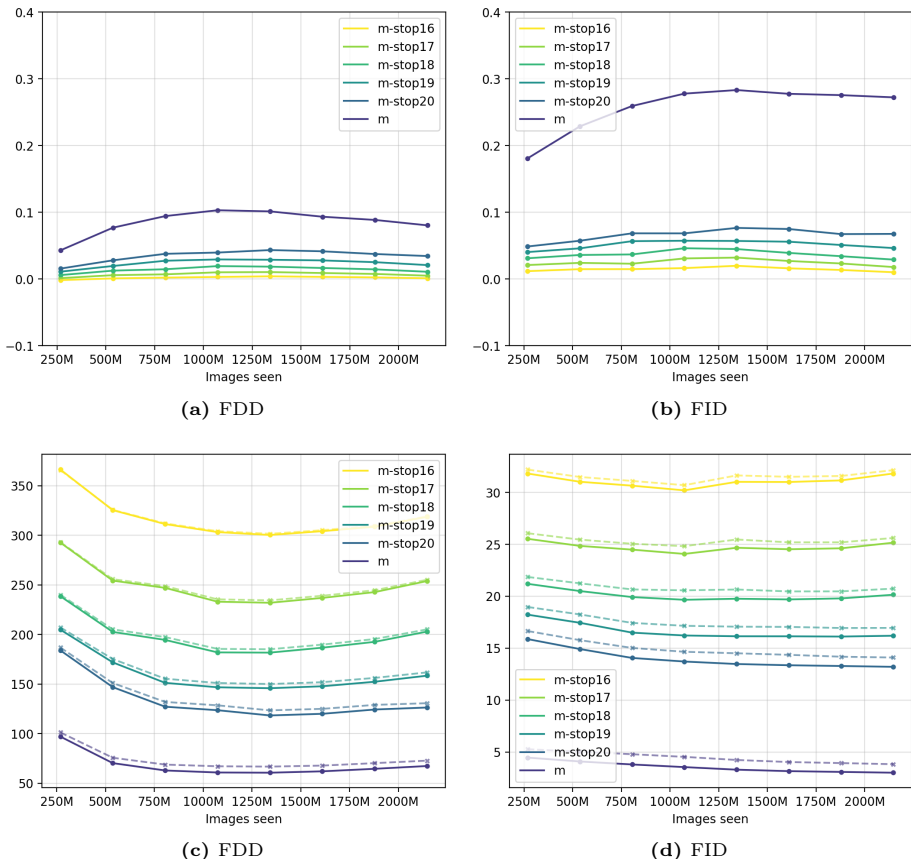


Fig. 10: (a)-(b) Relative generalization gap $(M_{val} - M_{train})/M_{train}$ and (c)-(d) training and validation results $M_{train/val}$, with EDM2-M on ImageNet-64 with tFD and truncated inference. The indices in the legend show at which step inference was stopped, with 16, 17, 18, 19, 20 corresponding to intermediate noise levels $\sigma \approx 2.2, 1.6, 1.2, 0.8, 0.6$, comparable to the peak in the relative generalization gap for the reconstruction-based metrics.

B Fréchet Distance details

B.1 Comparable FD protocol

Although FID and FDD are standard generative metrics in the literature, there is no standard protocol to ensure comparability across runs. FD-based metrics are known to have high variance when the sample sizes in the references are low [12]. Therefore, it is common practice to use $>10k$ generated samples and as many data samples, training or otherwise, as possible. While this approach mitigates limited-sample bias, it complicates experimental setups that require comparisons between runs, beyond model size and training length. Specifically,

comparing model performance on the training and validation splits requires an equal number of training and validation samples in each reference, which usually limits the number of samples per reference to the number of validation samples.

Consider three sets of generated images A, B , and C . In general, whenever we compare two FD results, $FD(A, B)$ vs $FD(A, C)$, their difference might be due to (i) a different number of images per class between B and C (class prior mismatch), (ii) a different number of samples between B and C , which changes the estimator variance, (iii) estimator noise because we have a limited number of samples or (iv) differences in the underlying distribution between B and C , e.g., for different models or because a training and validation split are not i.i.d.. To isolate model error, e.g., overfit, we need to control for the other factors, by (i) matching class priors, (ii) matching the number of samples between B and C (A and B , and A and C do not need to have the same number samples), and (iii) if possible, rerun with multiple i.i.d sets, e.g., different random seeds for models or different subsets of the training distribution.

To obtain results that are comparable between runs against the training reference and validation reference, our FD computation protocol on ImageNet was as follows:

1. We sampled 15 50k random subsets from the training split, with the same class prior as in the 50k validation split.
2. We used that class prior to generate 50k images per run.
3. We computed the FD of the generated set against all available subsets of the training and validation split and averaged the results across subsets.

On CIFAR-10/100, we follow the same protocol, but since the validation set is limited to 10k samples, we also limit the training subsets to 10k samples. We still use 50k generated images each time. The results on condition granularity use uniform sampling of the class label for each image, rather than fixing the prior, because models trained on different numbers of classes cannot be constrained to the same prior.

B.2 Training-validation mismatch on ImageNet

At least part of the generalization gaps we observe may be due to a slight distribution mismatch between the training and validation sets, arising from differences in the data collection process for ImageNet and for CIFAR-10/100, due to natural variance in global statistics on small datasets. To test this, we quantify mismatch and limited-sample bias by measuring the tFD between 50k subsets of the training data with the validation splits, and different training subsets, respectively (Tab. 2). See the supplementary material for a full description of the setup. We find that, regardless of the dataset, FDDs involving generated images are substantially higher than the natural split mismatch and limited-sample bias, ruling out that the gaps we observed in our previous analysis are due to distribution mismatches.

Because FD-based metrics are non-linear, we can't decompose the FD results for generated images into their components, thereby prohibiting further analysis. For FID, we observe very high baselines, only slightly below the results on generated data (Tab. 2), indicating that, with Inception-v3 features, biases other than non-i.i.d. data can easily dominate the outcome.

Table 2: Baseline Fréchet Distances. "Train" shows the average results between 20 different subsets of the training data. "Val" shows a single result between a training subset and the validation split. "Gen" shows the lowest values achieved by an EDM/EDM2 model.

Train-vs-	FDD			FID		
	Train	Val	Gen	Train	Val	Gen
ImageNet-64	13.5	20.6	>52	1.26	1.70	>2.8
ImageNet-512	12.9	26.2	>52	1.26	2.67	>2.6
CIFAR-10	-	31.2	>158	-	3.15	>3.8
CIFAR-100	-	37.4	>222	-	3.58	>4.5

C Long-range dependencies tend to be memorized

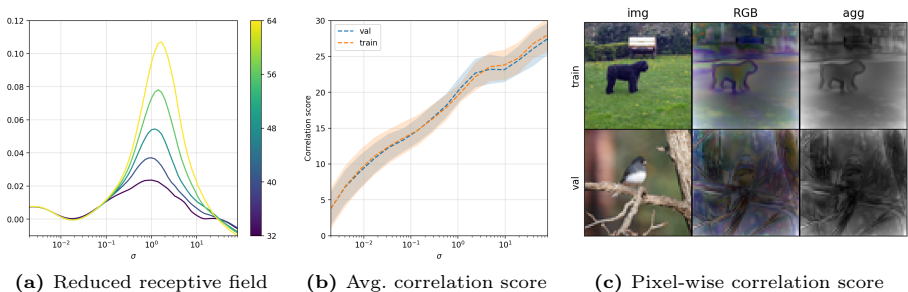


Fig. 11: (a) Decreasing the receptive field mitigates the relative generalization gap $(E_{val} - E_{train})/E_{train}$. Colorbar shows the sliding window size. 64 corresponds to regular inference. (b) During inference, the model shifts from long-range correlations to short-range correlations. The correlation score is averaged over pixels and images. (c) Edge pixels tend to have longer-range dependencies. $\sigma \approx 1.2$. RGB shows the pixel-wise correlation score, agg is aggregated over channels. All plots show ImageNet-64, EDM2-S.

Globally coherent images are more difficult to generate because features that require correct long-range pixel dependencies are highly image-specific and thus harder to generalize than local pixel patterns. Similar to training samples in sparsely supported regions of the input space, this should promote memorization of said features. To test this, we constrain the range of pixel dependencies the denoiser can model, following [2], by denoising smaller image patches of equal size and then composing them back together. Overlapping pixels are averaged. We find that this dramatically shrinks the generalization gap (Fig. 11a), supporting the hypothesis.

Further, we investigate how the denoising of each pixel is affected by other pixels, how these dependencies are distributed within an image, and how this relates to the noise level $\sigma(t)$. We define a pixel-level correlation score by computing the average gradient of a pixel in the denoised image with respect to all pixels in the input image, weighted by the L2 distance to those pixels. Specifically, given an image \mathbf{y} with N pixels, a denoiser $D(\cdot)$, noise level σ and noise $\boldsymbol{\eta} \sim \mathcal{N}(0, 1)$, we compute the correlation score of the ij -th pixel as

$$CS_{ij} = \frac{\frac{1}{N} \sum_{k,l} d(i, j, k, l) \frac{\partial D(\mathbf{x})_{ij}}{\partial \mathbf{y}_{kl}}}{\frac{1}{N} \sum_{k,l} \frac{\partial D(\mathbf{x})_{ij}}{\partial \mathbf{y}_{kl}}}, \quad \mathbf{x} = \mathbf{y} + \sigma \boldsymbol{\eta}$$

with $d(i, j, k, l) = \left\| \begin{pmatrix} i \\ j \end{pmatrix} - \begin{pmatrix} k \\ l \end{pmatrix} \right\|_2$ being the L2 distance between the ij -th and kl -th pixels. A larger correlation score for a given pixel indicates that the gradient activations are high for distant pixels. We find that, on average, the farther a pixel in the output image is from the center, the longer its dependencies extend across the input images (Fig. 11c, Fig. 12). In other words, the object determines the background, but the background does not determine the object. It is unclear how the dataset’s object-centric nature influences this result. When averaging the correlation scores across images, we see that as the noise level $\sigma(t)$ decreases, the distance of the average gradient signal across an image also decreases (Fig. 11b), i.e., the focus shifts from long-range dependencies to short-range dependencies during inference.

D Additional results for the relative generalization gap

This section presents the relative generalization gaps across all our metrics with the EDM2 [38] model on ImageNet-64/512 and the EDM [36] model on CIFAR-10/100, excluding results specific to condition granularity (Sec. F) and diffusion guidance (Sec. G).

D.1 ImageNet-64

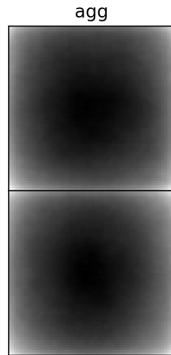


Fig. 12: Edge pixels tend to have longer-range dependencies. Shown is the pixel-wise correlation score, averaged over 128 images, computed with EDM2-S on ImageNet-64 at $\sigma = 1$.

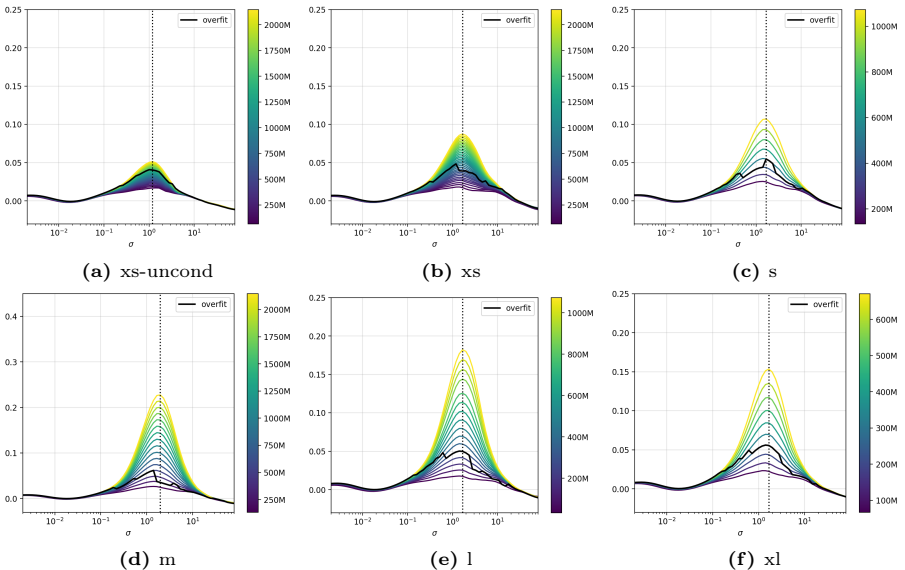


Fig. 13: Relative generalization gap $(E_{val} - E_{train})/E_{train}$ with EDM2 on ImageNet-64 for various model sizes. Black lines indicate σ values used in Fig. 15 and Fig. 16.

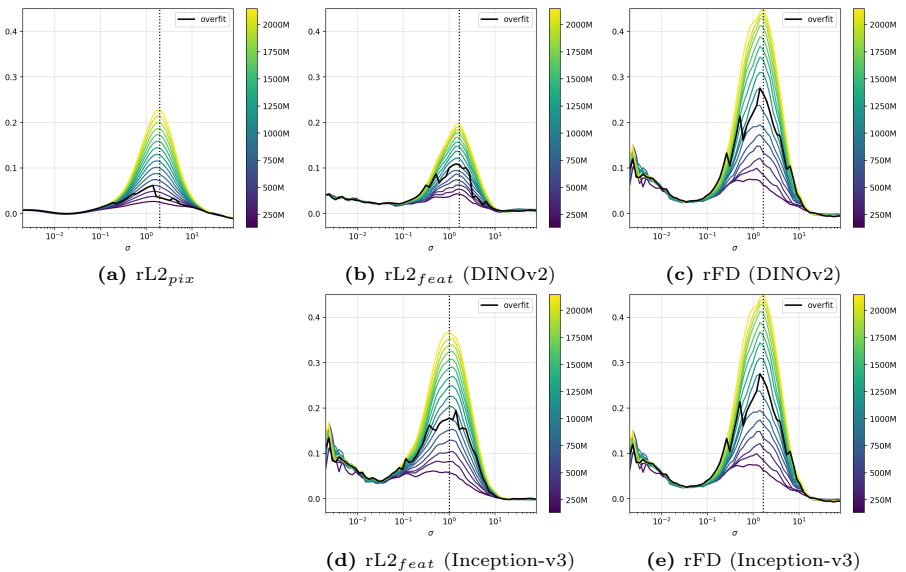


Fig. 14: Relative generalization gap $(M_{val} - M_{train})/M_{train}$ with EDM2-M on ImageNet-64 for various metrics. Black lines indicate σ values used in Fig. 15 and Fig. 16.

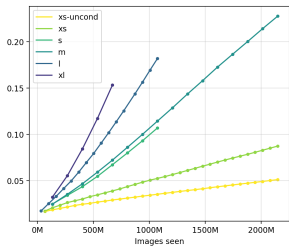
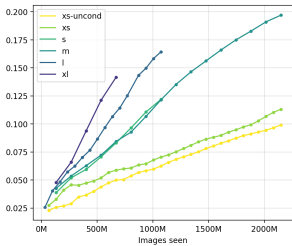
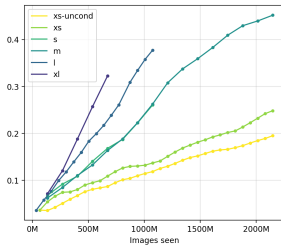
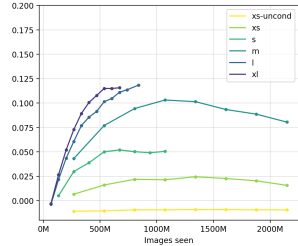
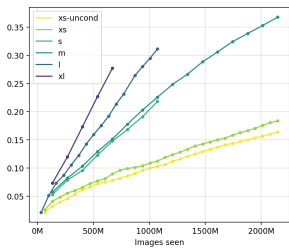
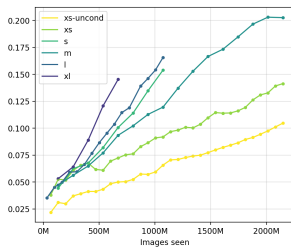
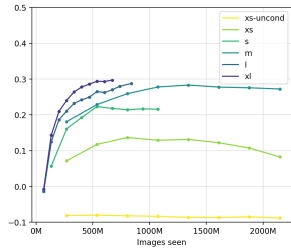
(a) $rL2_{pix}$ (b) $rL2_{feat}$ (DINOv2)(c) rFD (DINOv2)(d) tFD (DINOv2)(e) $rL2_{feat}$ (Inception-v3)(f) rFD (Inception-v3)(g) tFD (Inception-v3)

Fig. 15: Relative generalization gap $(M_{val} - M_{train})/M_{train}$ with EDM2 on ImageNet-64 for various metrics and model sizes. For reconstruction-based metrics, σ is fixed at the peak of the generalization gap, see Fig. 13 and Fig. 14.

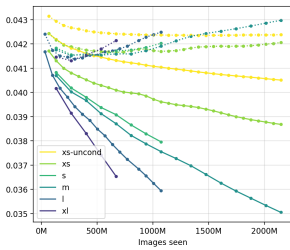
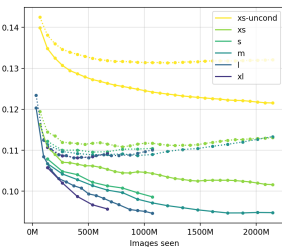
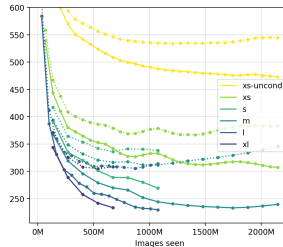
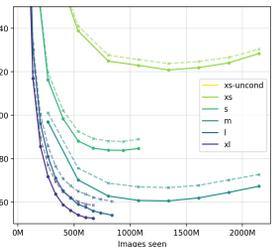
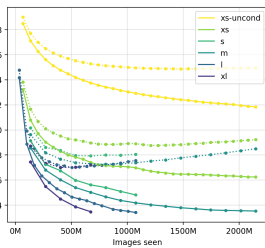
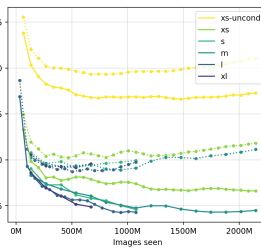
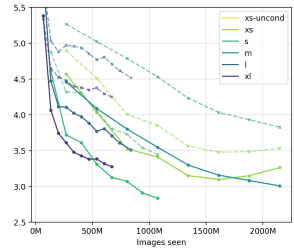
(a) $rL2_{pix}$ (b) $rL2_{feat}$ (DINOv2)(c) rFD (DINOv2)(d) tFD (DINOv2)(e) $rL2_{feat}$ (Inception-v3)(f) rFD (Inception-v3)(g) tFD (Inception-v3)

Fig. 16: Training and validation results $M_{train/val}$ with EDM2 on ImageNet-64 for various metrics and model sizes. For reconstruction-based metrics, σ is fixed at the peak of the generalization gap, see Fig. 13 and Fig. 14.

D.2 ImageNet-512

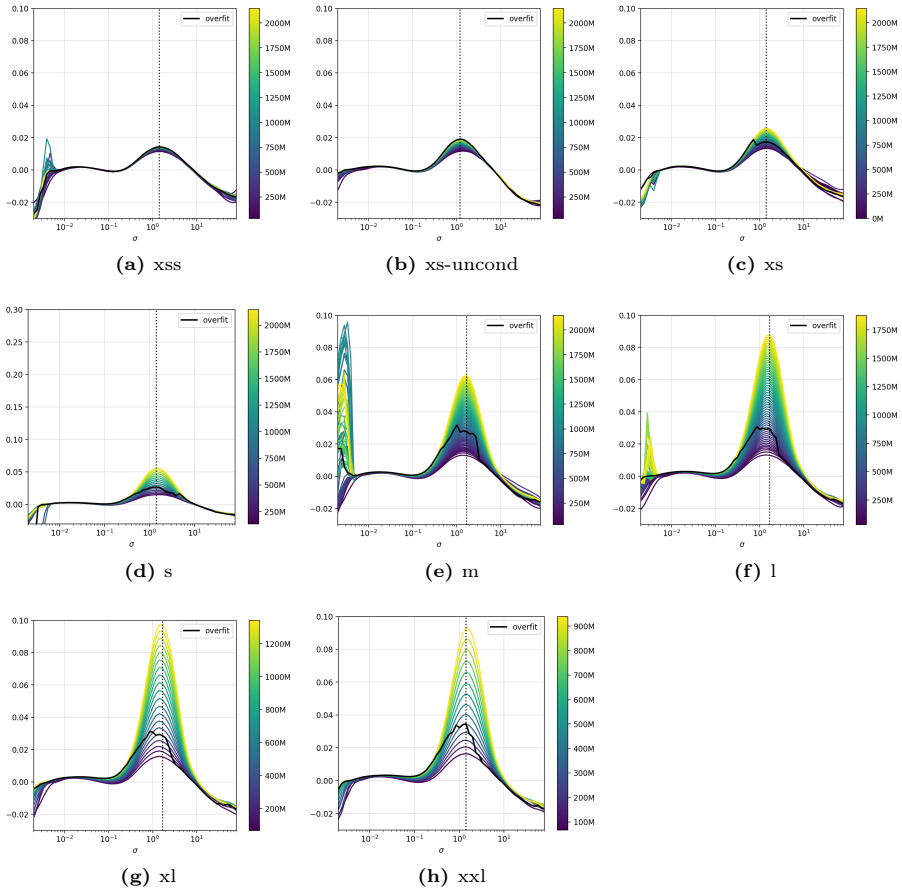


Fig. 17: Relative generalization gap $(E_{val} - E_{train})/E_{train}$ with EDM2 on ImageNet-512 for various model sizes. Black lines indicate σ values used in Fig. 19.

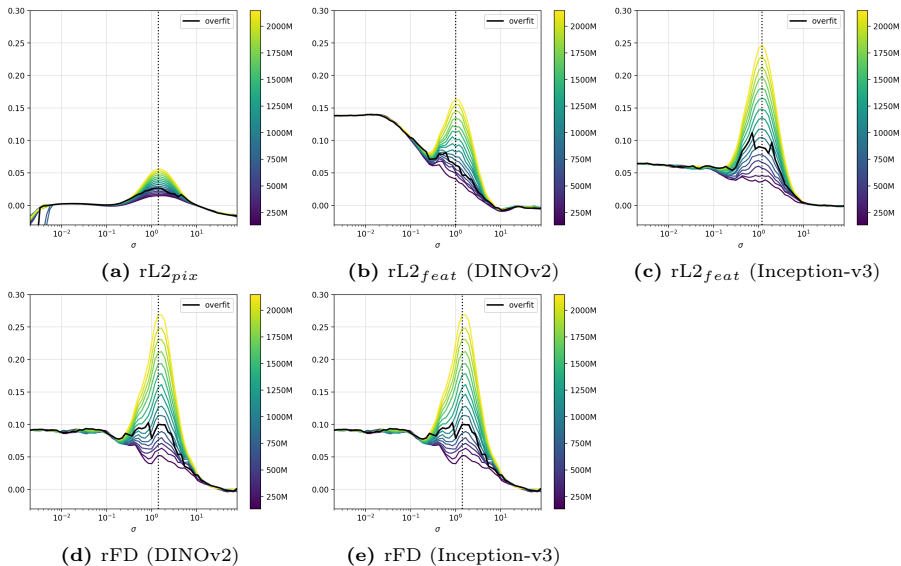


Fig. 18: Relative generalization gap $(M_{val} - M_{train})/M_{train}$ with EDM2-M on ImageNet-512 for various metrics. Black lines indicate σ values used in Fig. 19.

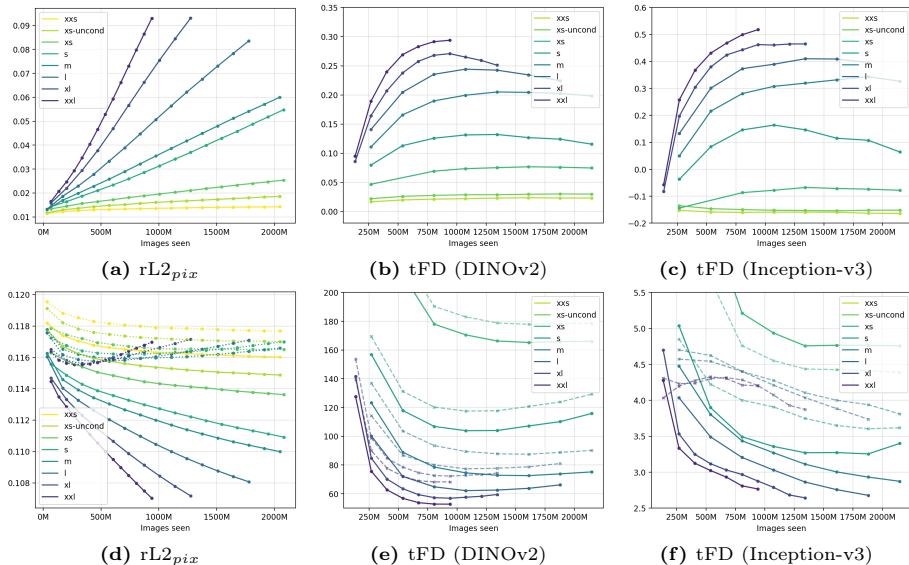


Fig. 19: (a)-(c) Relative generalization gap $(M_{val} - M_{train})/M_{train}$ and (d)-(f) training and validation results M_{train}/val , with EDM2 on ImageNet-512 for various metrics and model sizes. For $rL2_{pix}$, σ is fixed at the peak of the generalization gap, see Fig. 17 and Fig. 18.

D.3 CIFAR-10/100

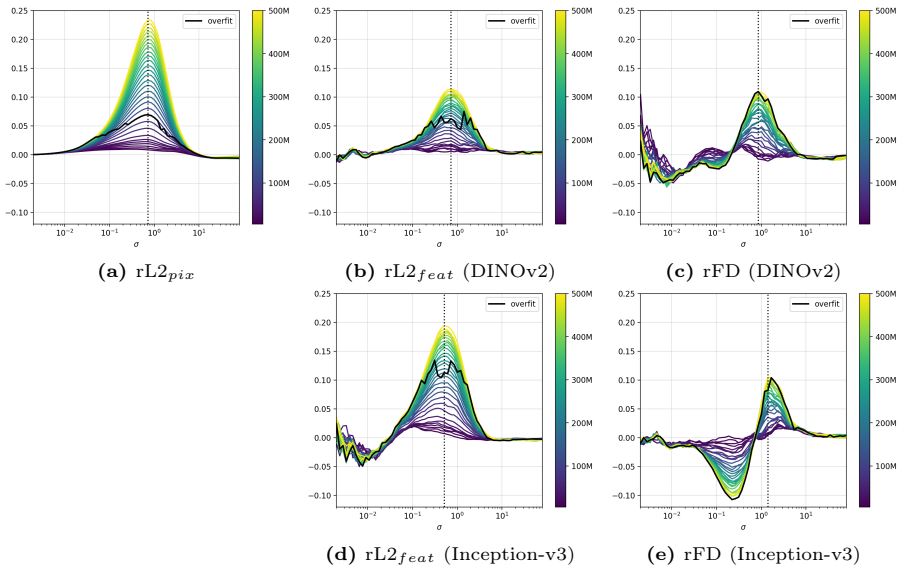


Fig. 20: Relative generalization gap $(M_{val} - M_{train})/M_{train}$ with EDM on CIFAR-10 for various metrics. Black lines indicate σ values used in Fig. 22 and Fig. 23.

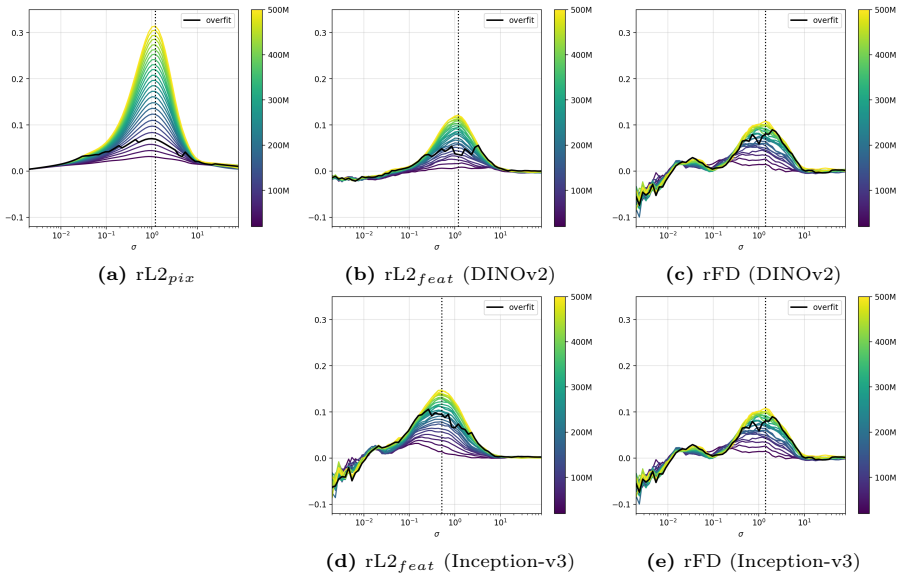
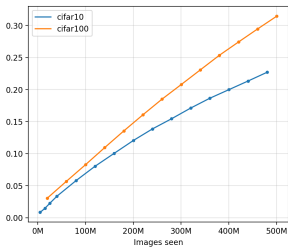
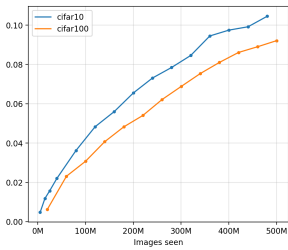
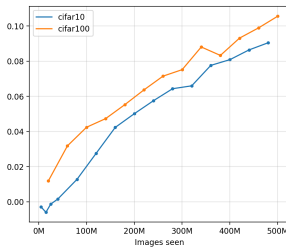
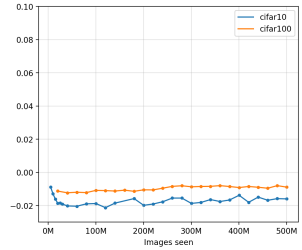


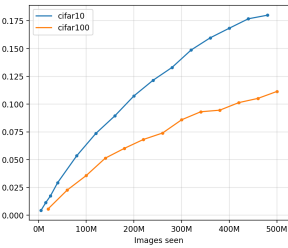
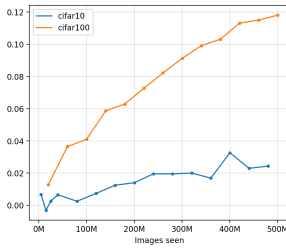
Fig. 21: Relative generalization gap $(M_{val} - M_{train})/M_{train}$ with EDM on CIFAR-100 for various metrics. Black lines indicate σ values used in Fig. 22 and Fig. 23.

(a) $rL2_{pix}$ (b) $rL2_{feat}$ (DINOv2)

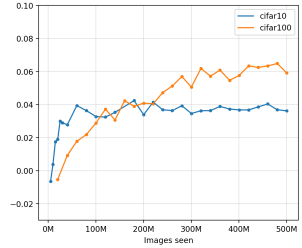
(c) rFD (DINOv2)



(d) tFD (DINOv2)

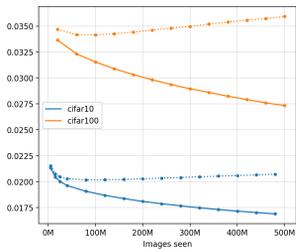
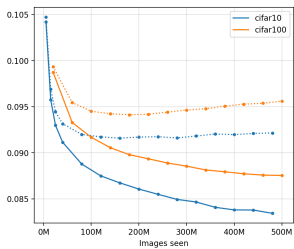
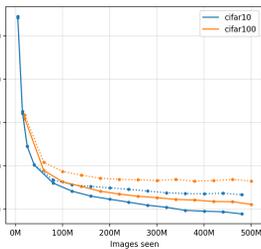
(e) $rL2_{feat}$ (Inception-v3)

(f) rFD (Inception-v3)

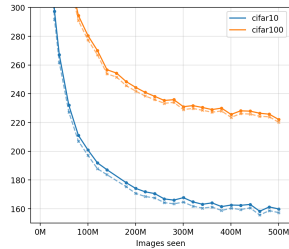


(g) tFD (Inception-v3)

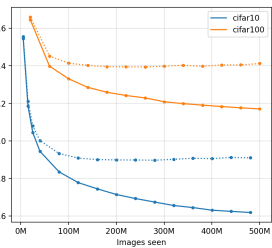
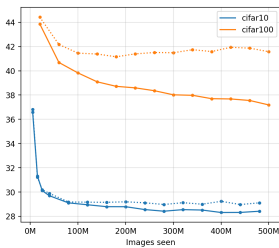
Fig. 22: Relative generalization gap $(M_{val} - M_{train})/M_{train}$ with EDM on CIFAR-10/100 for various metrics and model sizes. For reconstruction-based metrics, σ is fixed at the peak of the generalization gap, see Fig. 20 and Fig. 21.

(a) $rL2_{pix}$ (b) $rL2_{feat}$ (DINOv2)

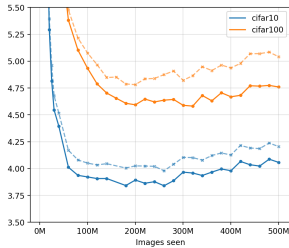
(c) rFD (DINOv2)



(d) tFD (DINOv2)

(e) $rL2_{feat}$ (Inception-v3)

(f) rFD (Inception-v3)



(g) tFD (Inception-v3)

Fig. 23: Training and validation results $M_{train/val}$ with EDM on CIFAR-10/100 for various metrics and model sizes. For reconstruction-based metrics, σ is fixed at the peak of the generalization gap, see Fig. 20 and Fig. 21.

E Toy model with random data

Instead of considering a symmetric distribution of N training points $\{y_i^{tr}\}_{i=1}^N$ and N validation points $\{y_i^{val}\}_{i=1}^N$, we consider a random distribution of those points on a circle. The results are qualitatively the same, although considerably noisier, depending on the random seed. Fig. 24 shows the flow field geometry for this setup. Note that, especially for small N , the superposition of all training points does not necessarily lie on the center of the circle (Fig. 24a), possibly causing the right-tail of the generalization gap to be different from 0 (Fig. 25)b. The manifold approximated by reconstructions at intermediate noise can have disconnected regions (Fig. 24b), where support is sparse, but densely populated regions collapse onto the training points later (Fig. 24c). The supplementary material includes a Jupyter Notebook that reproduces all figures related to the toy model and more.

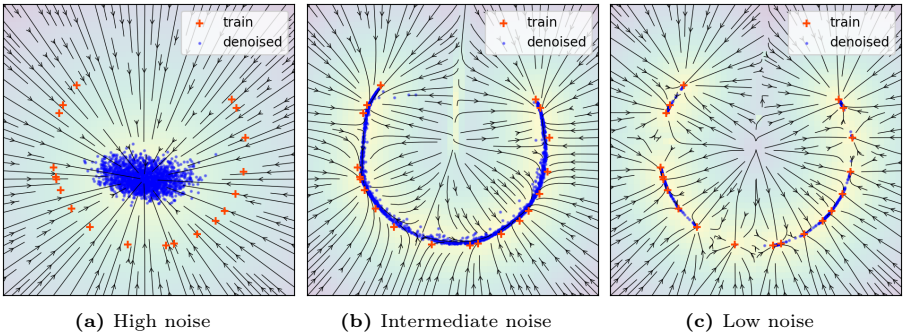


Fig. 24: Flow field lines and predictions of the optimal target predictor $\mathbf{y}^*(\mathbf{x}, \sigma)$ at different noise levels $\sigma = 28, 2.8, 0.63$. Color indicates the magnitude of the prediction error $\mathbf{y}^*(\mathbf{x}, \sigma) - \mathbf{x}$. Field geometry is (a) global, predictions tend towards the superposition of all training points. (b) moderately localized around training points, predictions approximate the data manifold (c) highly localized around each training point, predictions replicate the training points.

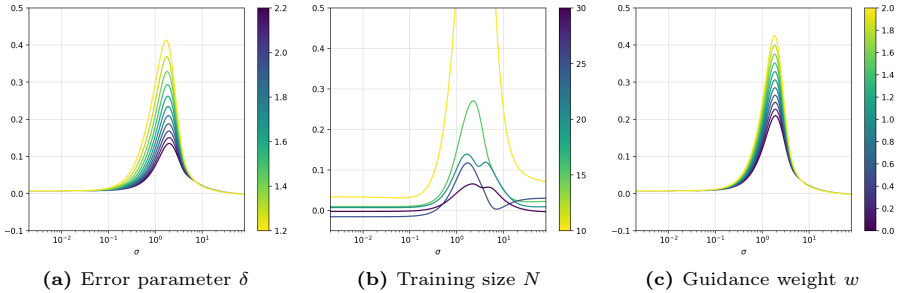


Fig. 25: Relative generalization gap $(E_{val} - E_{train})/E_{train}$ in our 2D toy model with random data and (a) different settings of the model error parameter δ , (b) different number of training points, and (c) different settings for the guidance weight w . $w = 0$ corresponds to no guidance.

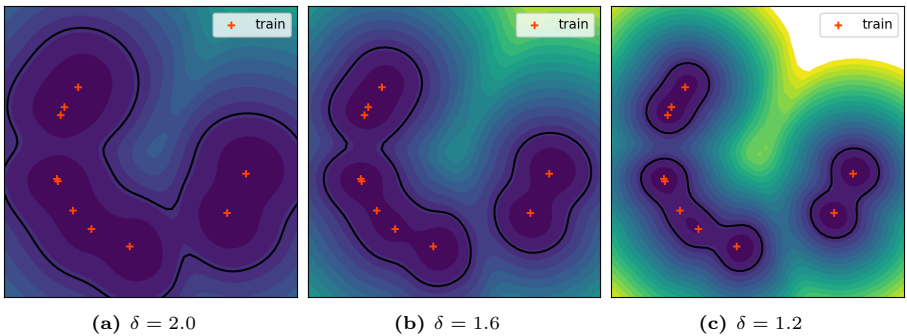
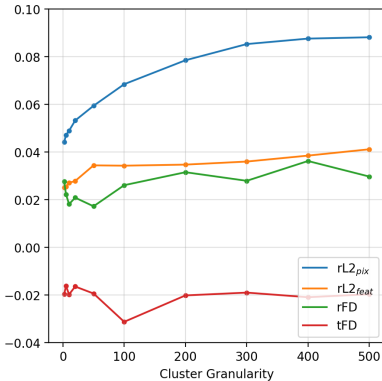


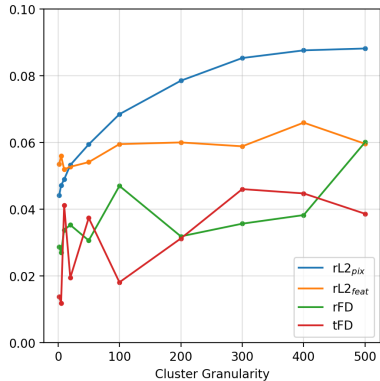
Fig. 26: Filled contours showing the relative generalization gap $(E - E_{train})/E_{train}$ at intermediate noise ($\sigma \approx 1.1$) between the training points and each point in space, respectively. The black lines enclose the area where this gap is 0.5 or less. As the model error δ decreases, this region shrinks until it no longer contains the validation points, indicating that the generalization gap to the validation set is larger than 0.5.

F Condition granularity results with Inception-v3

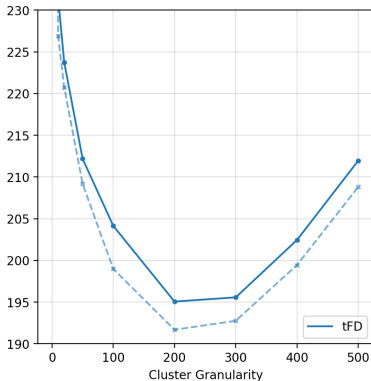
To test the sensitivity of the generalization behavior to condition granularity, we retrained EDM [36] on CIFAR-10 for 100M images across varying numbers of classes. Classes were computed algorithmically using k-means clustering in DINOv2 feature space. Results with Inception-v3 features are qualitatively similar to those with DINOv2 features.



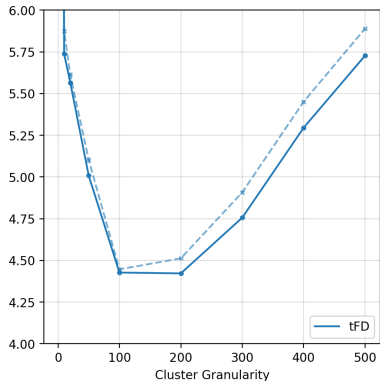
(a) DINOv2



(b) Inception-v3



(c) FDD



(d) FID

Fig. 27: (a)-(b) Relative generalization gap $(M_{val} - M_{train})/M_{train}$ for various metrics and (c)-(d) training and validation results $M_{train/val}$ with FDD/FID, with EDM on CIFAR-10. We retrained for 100Mimg (half of the default) with different numbers of classes. Classes were computed algorithmically using k-means clustering in DINOv2 feature space. For reconstruction-based metrics, σ is fixed at the peak of the generalization gap.

G More diffusion guidance results

We use both Autoguidance [37] and Classifier-Free Guidance [28] as they are implemented in the EDM2 [38] codebase. A guidance weight of $w = 0$ corresponds to no guidance. Results with Inception-v3 features are qualitatively similar to those with DINOv2 features.

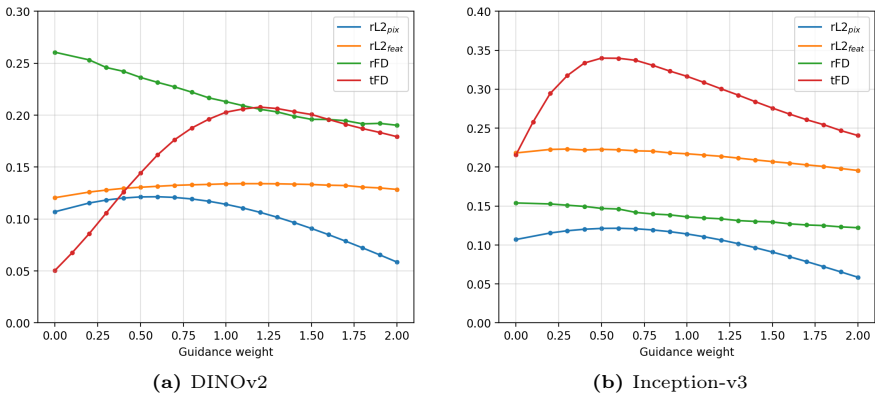


Fig. 28: Relative generalization gaps $(M_{val} - M_{train})/M_{train}$ with Autoguidance with EDM2-S on ImageNet-64. Reconstruction-based metrics fix σ at the peak of the generalization gap (see Fig. 30).

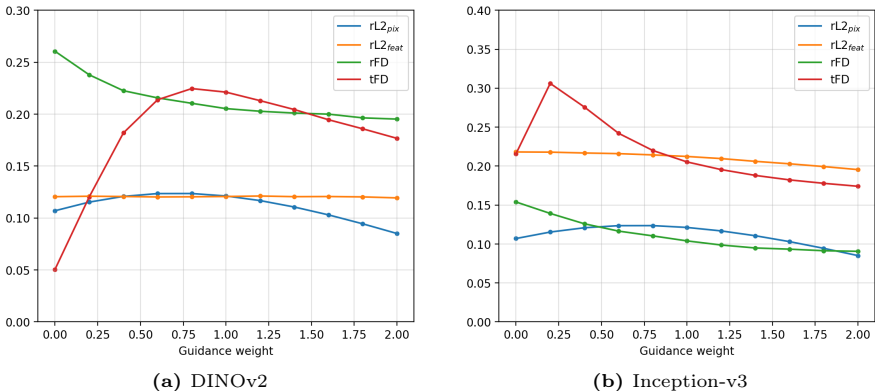


Fig. 29: Relative generalization gaps $(M_{val} - M_{train})/M_{train}$ with Classifier-Free Guidance with EDM2-S on ImageNet-64. Reconstruction-based metrics fix σ at the peak of the generalization gap (see Fig. 31).

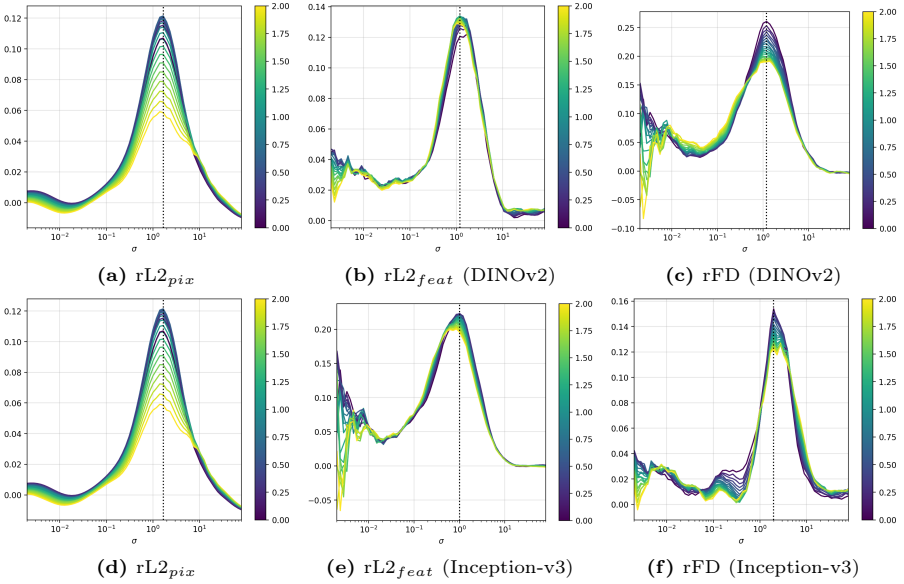


Fig. 30: Relative generalization gaps $(M_{val} - M_{train})/M_{train}$ with Autoguidance with EDM2-S on ImageNet-64. Black lines indicate σ values used in Fig. 28

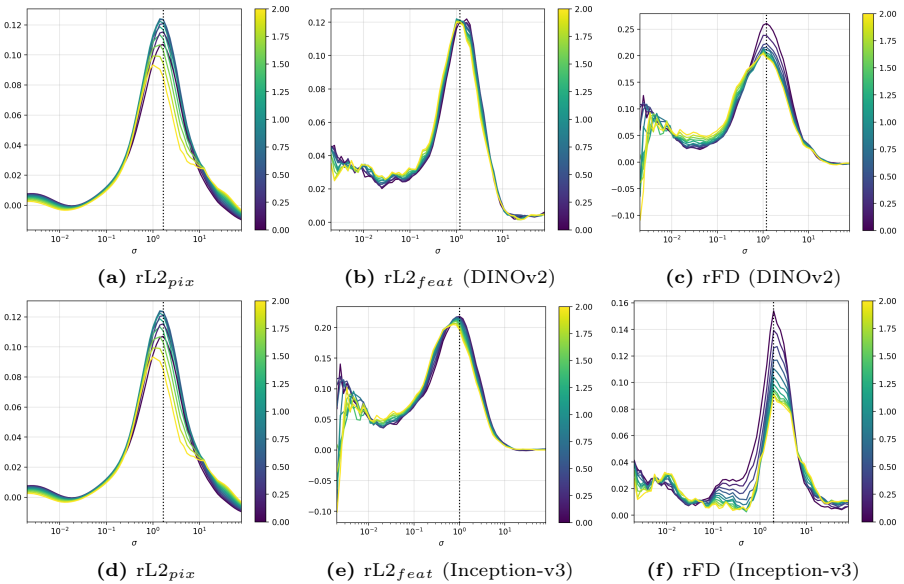


Fig. 31: Relative generalization gaps $(M_{val} - M_{train})/M_{train}$ with Classifier-Free Guidance with EDM2-S on ImageNet-64. Black lines indicate σ values used in Fig. 29